

Impurity-Induced Environmental Quantum Phase Transitions in the Quadratic-Coupling Spin-Boson Model

Da-Chuan Zheng,¹ Li Wan,² and Ning-Hua Tong^{1,*}

¹*Department of Physics, Renmin University of China, 100872 Beijing, China*

²*Department of Physics, Wenzhou University, 325035 Wenzhou, China*

(Dated: June 18, 2019)

We studied the zero temperature properties of the spin-boson model with quadratic spin-boson coupling. This model describes a superconducting qubit (spin) coupled to the circuit noise (bosons) at the optimal working point, and an impurity atom or quantum dot quadratically coupled to acoustic phonons. We show that quantum phase transitions can occur in the boson degrees of freedom, between a environment-stable state and a state with local environmental distortions. Using Wilson's numerical renormalization group method and the exact solution at the non-tunnelling limit $\Delta = 0$, we obtain the phase diagram that contains the first-order as well as continuous QPTs. The equilibrium state dynamical correlation functions of the spin and the bath are studied, showing the power-law ω -dependences at and away from the critical point. We discuss the relevance of these results to experiments.

PACS numbers: 05.10.Cc, 64.70.Tg, 03.65.Yz, 05.30.Jp

I. INTRODUCTION

The spin-boson model (SBM) is a frequently used paradigm to study the influence of the environmental noise on the quantum evolution of a two-level system [1–3]. The noise-induced dissipation and dephasing is the central issue of a variety of research fields, ranging from the electron/energy transfer in bio-chemical systems [4–7] to the endeavour of building a quantum computer [8–12]. Sufficiently strong coupling to the bosonic bath also induces a localize-delocalize quantum phase transition (QPT) in the two-level system [13–20]. The non-trivial universality class of this QPT receives much attention in recent years [21–25]. Experimental realization of the SBM have been proposed in various contexts, ranging from the mesoscopic metal ring to cold atom systems [26–29].

The conventional SBM, composed of a quantum spin linearly coupled to the displacement operator of a group of harmonic oscillators, belongs to the quantum impurity problem where the properties of the impurity is determined by the (infinitely) many degrees of freedom in the bath, but the influence of the impurity on the bath is negligibly small. Recently, much attention is paid to the quantum two-level system quadratically coupled to a bosonic environment. Such a problem arises in various qubit systems, including the superconducting qubit [30–34], semiconductor quantum dot [35], and the bismuth donors in silicon [36], where the linear qubit-environment coupling is tuned to zero to suppress the decoherence and the remaining leading order coupling is quadratic. Significant enhancement of the coherence time has been achieved at such an optimal working point. Theoretical studies have been carried out to understand the influence

of the quadratic coupling on the dephasing of the qubit [37–40]. In the quantum dot-based qubit systems, the quadratic electron-phonon coupling is derived to explain the anomalous temperature dependence of the absorption line shape [41, 42]. For the quantum Brownian motion of a heavy particle quadratically coupled to the environment, Maghrebi *et al.* suggested that the quadratic couplings leads to the anomalous diffusion of the particle [43].

As for the linear-coupling SBM, previous studies of the quadratic-coupling SBM focused mainly on the influence of the environment on the quantum two-level systems. However, in striking contrast to the linear-coupling case, the non-linearity of the spin-boson coupling makes the feedback effect of the impurity to the bath no longer negligible. Especially, the coupling quadratic in the coordinate of the environmental bosons will shift the boson energies and lead to new phenomenon such as the softening of the environmental bosons. In this paper, we show that a strong quadratic coupling can even induce a QPT in the environment and qualitatively change the bath. At the QPT, the environmental bosons become unstable with inverted harmonic potentials. Considering higher order anharmonic potentials, this will lead to a local distortion in the environment as the new state. We find that the ground state phase diagram includes both the first-order and continuous QPTs. As a consequence of the QPT, the quantum dynamics of both the spin and the bath are severely changed, at and away from the QPTs. This makes such QPTs an indispensable ingredient to consider in the study of the above-stated systems.

The rest of the paper is organized as the following. In Section II, we describe the model and the methods used to study it. Section III is devoted to the main results, including the exact solution at $\Delta = 0$ and the NRG results for $\Delta > 0$. Various related issues for the quadratic-coupling SBM are discussed in Section IV. The details of the exact solution at $\Delta = 0$ is presented in Appendix

*Electronic address: nhtong@ruc.edu.cn

A. The NRG formalism is summarized in Appendix B. In Appendix C, we present quantitative comparison between the NRG data and the exact solution for $\Delta = 0$.

II. MODEL AND METHODS

A general Hamiltonian describing a two-level system coupled to the environmental noise can be written as

$$H = \frac{\epsilon}{2}\sigma_z - \frac{\Delta}{2}\sigma_x + \sum_i \omega_i a_i^\dagger a_i + \frac{1}{2}\sigma_z f(\hat{Y}), \quad (1)$$

where $\hat{Y} = \sum_i \lambda_i(a_i + a_i^\dagger)$ is the local boson displacement operator. λ_i describes the local weight of the i -th boson mode. The two-level system is represented by a spin 1/2 with bias ϵ and tunnelling strength Δ . It is coupled to the bosonic bath with mode energies $\{\omega_i\}$ in terms of σ_z and \hat{Y} . In the weak coupling limit, the function $f(z)$ can be expanded into Taylor series $f(z) = g_0 + g_1 z + g_2 z^2 + \dots$. The conventional SBM Hamiltonian is obtained by truncating the series at the linear order. At the optimal point of the superconducting qubit experiments [30–36], the linear coupling g_1 is tuned to zero and the leading contribution to the coupling is quadratic in the boson coordination [37]. Truncating the series at this order and absorbing the constant g_0 into ϵ , we obtain the Hamiltonian of the quadratic-coupling SBM as

$$H_{QSB} = \frac{\epsilon}{2}\sigma_z - \frac{\Delta}{2}\sigma_x + \sum_i \omega_i a_i^\dagger a_i + \frac{g_2}{2}\sigma_z \hat{Y}^2. \quad (2)$$

The effect of the bath on the spin is encoded into the bath spectral function $J(\omega)$ which is defined as

$$J(\omega) = \pi \sum_i \lambda_i^2 \delta(\omega - \omega_i). \quad (3)$$

The coupling constant g_2 can be absorbed into $J(\omega)$, or equivalently, is set as unity in the numerical calculation below. We consider a power law form of $J(\omega)$ in the low frequency limit with a hard cut-off at ω_c ,

$$J(\omega) = 2\pi\alpha\omega^s\omega_c^{1-s}, \quad (0 \leq \omega \leq \omega_c). \quad (4)$$

Here α controls the strength of the spin-boson coupling. The exponent s is determined by the distribution of energies ω_i and weights λ_i . $\omega_c = 1.0$ is set as the energy unit. In this work, we focus mainly on the effect of sub-Ohmic bath with $0 \leq s < 1$ and will discuss the result for Ohmic ($s = 1$) and super-Ohmic ($s > 1$) baths in the end of section III.

Here we compare the symmetry of H_{QSB} to that of the linear-coupling SBM H_{SB} . At $\epsilon = 0$, H_{SB} is invariant under the combined boson and spin transformation $Ua_iU^{-1} = -a_i$ and $U\sigma_zU^{-1} = -\sigma_z$. Previous studies disclosed that for the sub-Ohmic ($0 \leq s < 1$) and the Ohmic ($s = 1$) baths, a strong coupling strength may

induce a spontaneous breaking of this symmetry and the system enters the localized phase, in which the quantum system is trapped to one of the two states and the local bosons has a finite displacement [13, 14]. The transition is the so-called delocalize-localize transition of the SBM.

The Hamiltonian of the quadratic-coupling SBM Eq.(2) is invariant under the parity transformation $Ua_iU^{-1} = -a_i$ alone. In case the spin is in the state $\sigma_z < 0$, the quadratic coupling contributes a negative boson energy proportional to $-\hat{Y}^2$ which, when overcoming the energy ω_i of the low energy boson modes, may lead to an instability of the bosons. Physically, as the coupling strength increases, the harmonic potentials of the environmental particles are softened and the instability occurs at the potential inversion, accompanied with the divergence of particle numbers. A spontaneous breaking of the boson parity symmetry may occur at this transition. Under the constraints of higher order anharmonic potential of bosons beyond H_{QSB} , this instability will lead to a local distortion in the environmental degrees of freedom. Even for a weak quadratic coupling strength, the feedback effect of the impurity to the bath can no longer be regarded as small and the bath is intrinsically non-Gaussian. New dynamical behaviour will thus emerge both in the bath and the impurity.

At the non-tunnelling point $\Delta = 0$, the z -component of the spin has no dynamics. The eigen-states of H_{QSB} are in the form $|\Psi^{(+1)}\rangle|+1\rangle$ and $|\Psi^{(-1)}\rangle|-1\rangle$. $|+1\rangle$ and $| -1\rangle$ are eigen-states of σ_z with energies +1 and -1, respectively. $|\Psi^{(\pm 1)}\rangle$ are the corresponding boson states. In each spin sector, the quadratic boson Hamiltonian can be solved exactly. We use the equation of motion method for the double-time Green's functions to obtain the exact properties of H_{QSB} at $\Delta = 0$. The derivation is summarized in Appendix A.

For general parameters, we study H_{QSB} using the Wilson's numerical renormalization group (NRG) method [44, 45] adapted to the bosonic bath [13, 14]. The Wilson chain Hamiltonian can be derived from an orthogonal transformation of the logarithmic-discretized bath. It is given as

$$H_{NRG} = \frac{\epsilon}{2}\sigma_z - \frac{\Delta}{2}\sigma_x + \sum_{n=0}^{\infty} \left[\epsilon_n b_n^\dagger b_n + t_n \left(b_n^\dagger b_{n+1} + b_{n+1}^\dagger b_n \right) \right] + \frac{g_2}{2} \frac{\eta_0}{\pi} \sigma_z \hat{X}^2. \quad (5)$$

Here $\epsilon_n, t_n \propto \Lambda^{-n}$ are the on-site and hopping energies of the boson chain and $\Lambda \geq 1$ is the logarithmic discretization parameter. The displacement operator \hat{Y} in Eq.(2) is normalized as $\hat{Y} = \sqrt{\eta_0/\pi} \hat{X}$ with $\hat{X} = b_0 + b_0^\dagger$. The local boson annihilation operator reads

$$b_0 = \sqrt{\frac{\pi}{\eta_0}} \sum_i \lambda_i a_i. \quad (6)$$

Here $\eta_0 = \pi \sum_i \lambda_i^2 = \int_0^\infty J(\omega) d\omega$. The formalism used for NRG calculation is summarized in Appendix B.

Thanks to the exponential decay of energy scales along the chain, the low energy eigen-energies and eigen-states of H_{NRG} can be obtained reliably by iteratively diagonalizing H_{QSB} and keeping the lowest M_s states after each diagonalization. For each boson site to be added into the chain, we truncate its infinite dimensional Hilbert space into a N_b -dimensional space on the occupation number basis. The accuracy of NRG result is controlled by three parameters: the logarithmic discretization parameter Λ , the number of kept states M_s , and the boson-state truncation parameter N_b . In this work, the exact results at $\Lambda = 1.0$, $M_s = \infty$, and $N_b = \infty$ are produced by extrapolating the NRG data obtained using $\Lambda = 1.6 \sim 10.0$, $M_s = 60 \sim 300$, and $N_b = 8 \sim 50$ to the above limit.

III. RESULTS

As analysed above, the quadratic-coupling SBM has an impurity-induced QPT in the environmental degrees of freedom, at which the boson parity symmetry is broken. An interesting feature of H_{QSB} is that many of the universal properties of this non-trivial QPT are already well-described by the exactly soluble point $\Delta = 0$. A finite quantum tunnelling $\Delta > 0$ introduces non-trivial dynamics of σ_z and modifies the phase diagram from the $\Delta = 0$ limit. Below, we first focus ourselves on the point $\Delta = 0$, presenting the exact solution as well as the NRG results. Then, we use NRG to study the effect of finite quantum tunnelling $\Delta > 0$.

A. Non-tunnelling point $\Delta = 0$

The Hamiltonian H_{QSB} at $\Delta = 0$ reads

$$H_{QSB}(\Delta = 0) = \frac{\epsilon}{2}\sigma_z + \sum_i \omega_i a_i^\dagger a_i + \frac{g_2\eta_0}{2\pi}\sigma_z \hat{X}^2. \quad (7)$$

Here \hat{X} is the normalized boson displacement operator defined in Eq.(5). At this exact soluble limit, the dephasing properties were analysed in the context of the superconducting qubit at the optimal working point [37] and the quantum dot qubit quadratically coupled to acoustic phonons [41]. As confirmed by our NRG calculation below, the universal critical properties of the QPTs in H_{QSB} are already well described by this limit.

1. exact solution for $\Delta = 0$

To detect the environmental QPT, we calculate the zero-temperature dynamical correlation function $C_X(\omega)$ defined as

$$C_X(\omega) = \frac{1}{2\pi} \int_{-\infty}^{+\infty} C_X(t) e^{i\omega t} dt \quad (8)$$

with $C_X(t) \equiv (1/2)\langle\{X(t), X(0)\}\rangle$. We calculate the exact expression for $C_X(\omega)$ and the energy difference $\Delta E_g \equiv E_g^{(+1)} - E_g^{(-1)}$ between the two subspaces $\sigma_z = +1$ and $\sigma_z = -1$, from which the exact ground state phase diagram can be extracted. Using the Green's function equation of motion method, we obtain the exact expression for $C_X(\omega)$ at $T = 0$ as (see Appendix A for details),

$$C_X(\omega) = \frac{\frac{1}{2\eta_0} J(\omega)}{\left\{1 - g_2 \frac{\eta_0}{\pi} \sigma_z [g(\omega) + g(-\omega)]\right\}^2 + g_2^2 J^2(\omega)} \quad (9)$$

for $\omega > 0$. For $\omega < 0$, $C_X(\omega) = C_X(-\omega)$. The function $g(\omega)$ is given as

$$g(\omega) = \frac{1}{\eta_0} \mathcal{P} \int_0^\infty \frac{J(\epsilon)}{\omega - \epsilon} d\epsilon. \quad (10)$$

For the specific $J(\omega)$ given in Eq.(4), $\eta_0 = 2\pi\alpha\omega_c^2/(1+s)$ and the above equation simplifies into

$$g(\omega) = \frac{1}{\omega} F(1, 1+s; 2+s; \frac{\omega_c}{\omega}). \quad (11)$$

Here $F(\alpha, \beta; \gamma; z)$ is the hypergeometric function.

It is noted that $C_X(\omega)$ describes the effective spectral function of bosons renormalized by the impurity-bath coupling. In the weak coupling limit $\alpha = 0$, $C_X(\omega) = J(\omega)/(2\eta_0)$ recovers the normalized bare spectral function. A finite quadratic coupling to the impurity exerts significant influence on $C_X(\omega)$. Especially, an environmental QPT occurs when a singularity develops in $C_X(\omega = 0)$. Using the analytical continuation of $F(\alpha, \beta; \gamma; z)$ from $|z| > 1$ to $|z| < 1$, and considering $F(\alpha, \beta; \gamma; z = 0) = 1$, a continuous QPT is found at $\alpha_c = s/(4g_2\omega_c)$ in the subspace $\sigma_z = -1$ and no QPT occurs for $\alpha > 0$ in the other subspace $\sigma_z = +1$. The asymptotic behaviour of $C_X(\omega)$ in the small frequency limit reads

$$C_X(\omega) = \begin{cases} \frac{2(1+s)}{\pi^2 s^2} \frac{1}{\omega_c} \left(\frac{\omega}{\omega_c}\right)^{-s}, & (\alpha = \alpha_c); \\ \frac{(1+s)\alpha_c^2}{2(\alpha_c - \alpha)^2} \frac{1}{\omega_c} \left(\frac{\omega}{\omega_c}\right)^s, & (\alpha < \alpha_c). \end{cases} \quad (12)$$

For $\alpha \lesssim \alpha_c$, $C_X(\omega) \sim (\omega/\omega_c)^s$ for $\omega \ll \omega^*$ and $C_X(\omega) \sim (\omega/\omega_c)^{-s}$ for $\omega \gg \omega^*$. The peak position ω^* is given as

$$\omega^* = \omega_c \left(\frac{4}{\pi^2 s^2 \alpha_c^2}\right)^{\frac{1}{2s}} (\alpha_c - \alpha)^{\frac{1}{s}}, \quad (\alpha < \alpha_c). \quad (13)$$

It corresponds to the crossover energy scale T^* between the boson-stable state and the quantum critical regime. As α approaches α_c from below, the peak position moves to zero frequency in a power law $\omega^* \propto (\alpha_c - \alpha)^{z\nu}$, giving the exact exponent $z\nu = 1/s$.

The difference in the ground state energies of the two subspaces, $\Delta E_g = E_g^{(+1)} - E_g^{(-1)}$, is obtained as

$$\Delta E_g = \epsilon + \frac{1}{\pi} \int_{-\infty}^0 \text{Im}H(\omega + i\eta) d\omega, \quad (14)$$

in which

$$H(\omega) = \frac{2g_2/\pi}{1 - (2g_2/\pi)^2 h^2(\omega)} [h(\omega) + k(\omega)], \quad (15)$$

and

$$\begin{aligned} h(\omega) &= \int_{-\infty}^{\infty} \frac{J(\epsilon)\epsilon}{\omega^2 - \epsilon^2} d\epsilon, \\ k(\omega) &= \int_{-\infty}^{\infty} \frac{J(\epsilon)\epsilon}{(\omega - \epsilon)^2} d\epsilon. \end{aligned} \quad (16)$$

For a fixed coupling strength α , $E_g^{(+1)} < E_g^{(-1)}$ for very large negative ϵ . $E_g^{(+1)}$ increases with increasing ϵ until a level crossing occurs at ϵ_f , where the global ground state change from the subspace $\sigma_z = 1$ to $\sigma_z = -1$. The spin-flip transition line $\epsilon_f(\alpha)$ is determined by $\Delta E_g(\epsilon_f) = 0$. Taylor expanding ΔE_g with respect to α , one obtains in the small α limit

$$\epsilon_f = -\frac{2\alpha}{1+s}(g_2\omega_c^2) + \mathcal{O}(\alpha^3). \quad (17)$$

As will be shown below, this transition from $\langle \sigma_z \rangle = 1$ to $\langle \sigma_z \rangle = -1$ is abrupt only at $\Delta = 0$. For $\Delta > 0$, due to the mixing of spin-up and spin-down sub-spaces, this spin flip is not a phase transition but a smooth change without singularity.

2. NRG results for $\Delta = 0$

In this section, we present the NRG results for $\Delta = 0$ and compare them with the exact solution. The purpose is to benchmark the NRG method and gain further insight into the phase diagram at $\Delta = 0$. For simplicity, we present results only for a generic sub-Ohmic spectral function $J(\omega)$ with $s = 0.3$. Unless specified otherwise, qualitatively similar results are obtained for other s values. In our calculation we use $g_2 = 1.0$ and set $\omega_c = 1.0$ as the energy unit.

Fig.1 shows the ground state phase diagram on the $\alpha - \epsilon$ plane. Phase boundaries are obtained using NRG with $N_b = 8$ and 12. There are three phases characterized by $\langle S_z \rangle = \pm 1/2$ and $\langle X \rangle = 0$ or $\langle X \rangle \neq 0$. In the small α regime, the environmental bosons are in their stable state with $\langle X \rangle = 0$. For a fixed α in this regime, the ground state energies $E_g^{(+1)}$ and $E_g^{(-1)}$ changes with ϵ . When ϵ exceeds ϵ_f (up triangles), the two energies cross and it makes a spin flip from $\langle S_z \rangle = 1/2$ to $\langle S_z \rangle = -1/2$. In the large α regime, the boson parity symmetry is spontaneously broken and the order parameter $\langle X \rangle \neq 0$. The environmental stable and the unstable phases are separated by a vertical continuous transition line (circles) at $\alpha = 0.0786$ for larger ϵ , and by a first-order transition line (squares) for smaller ϵ . The three transition lines meet at a tri-critical point ($\alpha_c = 0.0786$, $\epsilon_c = -0.1273$) (solid dot in Fig.1).

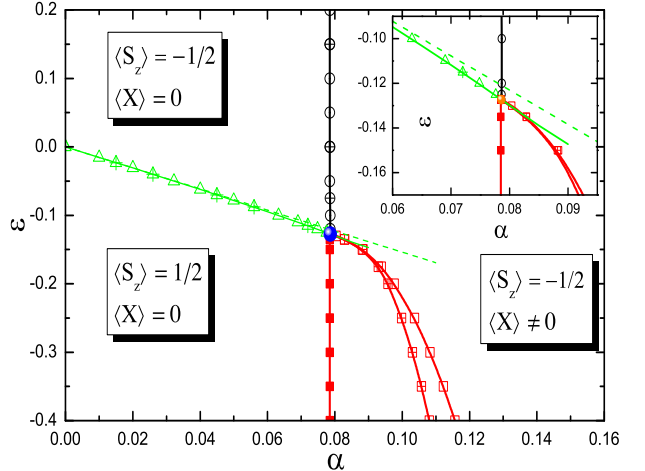


FIG. 1: Ground state NRG phase diagram of $H_{QSB}(\Delta = 0)$ for $S = 0.3$. $\langle X \rangle = \langle b_0^\dagger + b_0 \rangle$ is the order parameter and $\langle S_z \rangle = \langle \sigma_z \rangle / 2$ is the spin polarization. The phase boundaries are obtained using $N_b = 8$ (empty symbols) and $N_b = 12$ (plus-filled symbols). The circles, squares, and up triangles represent the continuous environmental, the first-order environmental, and the abrupt spin flip transitions, respectively. The vertical line with solid squares denote the first-order transition line extrapolated to $N_b = \infty$. The lines are for guiding eyes. The solid dot at $(\alpha_c = 0.0786, \epsilon_c = -0.1273)$ marks the tri-critical point. Inset: details of the spin flip line. The dashed line is $\epsilon = -2\alpha/(1+S)$ and the solid line is the exact spin flip transition line ϵ_f . Other NRG parameters are $\Lambda = 2.0$ and $M_s = 60$.

The inset of Fig.1 compares the NRG results obtained using $N_b = 8$ and $\Lambda = 2.0$ (up triangles) with the exact line of ϵ_f solved from $\Delta E_g = 0$ (solid line). The very good agreement is due to the cancellation of errors of $E_g^{(+1)}$ and $E_g^{(-1)}$ in the NRG calculation, since the error in the NRG ground state energy comes from its treatment of bosons, independent of the spin state.

The first-order QPT is a level crossing induced by the boson instability transition in the subspace $\sigma_z = -1$. For $\epsilon < \epsilon_c$ and small α , the subspace $\sigma_z = -1$ has higher energy than the $\sigma_z = 1$ subspace. As α approaches the boson instability point α_c , $E_g^{(-1)}$ drops to $-\infty$ abruptly while $E_g^{(+1)}$ is unchanged, leading to a sharp level crossing between the two ground states.

We use $\alpha_c^{(1)}$ and $\alpha_c^{(c)}$ to denote the first-order and the continuous QPT points, respectively. The above scenario of the QPTs suggests $\alpha_c^{(1)} = \alpha_c^{(c)} = \alpha_c$ for $\Delta = 0$. Here α_c is the critical point in the $\sigma_z = -1$ subspace and it is independent of ϵ . Indeed, NRG gives a vertical continuous QPT line at $\alpha_c^{NRG} = 0.0786$. It is slightly larger than $\alpha_c^{exc} = s/(4g_2\omega_c) = 0.075$ due to the logarithmic discretization error at $\Lambda = 2.0$. For the first-order transition line, NRG gives an ϵ -dependent $\alpha_c^{(1)}$ and it shifts to the left from $N_b = 8$ to $N_b = 12$. As shown in Fig.13 of Appendix C, in the limit $N_b \rightarrow \infty$, the line of $\alpha_c^{(1)}$ con-

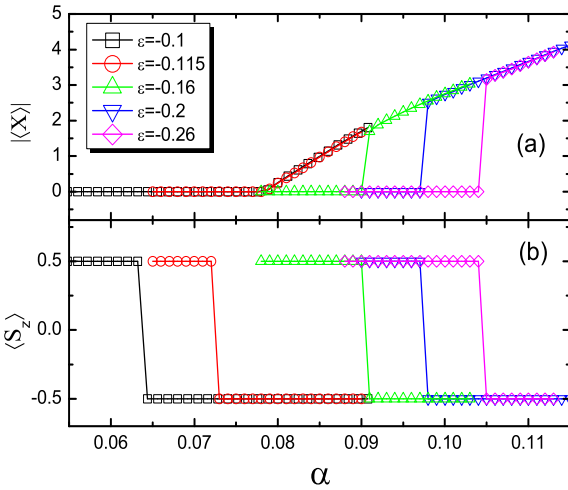


FIG. 2: NRG results for $|\langle X \rangle|$ and $\langle S_z \rangle$ as functions of α for $s = 0.3$ and $\Delta = 0.0$, for various ϵ values. The NRG parameters are $\Lambda = 2.0$, $M_s = 60$ and $N_b = 8$.

verges to the vertical line at $\alpha = \alpha_c^{(c)}$ (solid squares in Fig.1). Extrapolating the N_b -converged lines to $\Lambda = 1.0$ gives quantitative agreement with the exact value α_c^{exc} , as shown in Fig.12 of Appendix C.

In Fig.2, $\langle X \rangle$ and $\langle S_z \rangle$ are plotted as functions of α for various ϵ values. For $\epsilon = -0.1$ and -0.115 which are larger than ϵ_c , a spin-flip transition and a continuous QPT occur successively as α increases. For $\epsilon = -0.16$, -0.2 , and -0.26 which are smaller than ϵ_c , both quantities jump discontinuously at $\alpha_c^{(1)}$. It is noted that Fig.2 is a qualitative demonstration of the change of $\langle X \rangle$ only. In the limit $N_b = \infty$, as shown in Fig.11 and Fig.13 in Appendix C, $|\langle X \rangle|$ diverges both at the continuous and the first-order QPTs, being consistent with the scenario of the QPTs presented above.

As a direct product from NRG, the flow of the excitation energy levels can help identify various fixed points in the phase diagram, which is not directly addressed by the exact solution Eqs.(9)-(16). As shown in Fig.3, we found three distinct fixed points for $\epsilon = 0.1 > \epsilon_c$. The stable fixed point obtained for $\alpha = 0.084 < \alpha_c^{(c)}$ is identified as the free boson fixed point with $\langle X \rangle = 0$ and $\langle S_z \rangle = -1/2$. For $\alpha = 0.086 > \alpha_c^{(c)}$, the excitation energies flow towards a state with two-fold degeneracy. At this fixed point, the harmonic potential of bath particles is inverted and \hat{X} fluctuates between $\pm\infty$. In the large N regime, the degeneracy will be split by the numerical error, breaking the boson parity symmetry and giving $\langle X \rangle \neq 0$ [46]. At $\alpha = \alpha_c^{(c)}$, the excitation energies flow to an unstable critical fixed point and $\langle X \rangle$ becomes nonzero continuously at this point.

Fig.4 further discloses the nature of the strong-coupling fixed point. Here we plot $E_i(N)$ ($i = 1 \sim 6$), the eigen-energies directly obtained from diagonalizing the Wilson chain Hamiltonian H_N , without subtracting

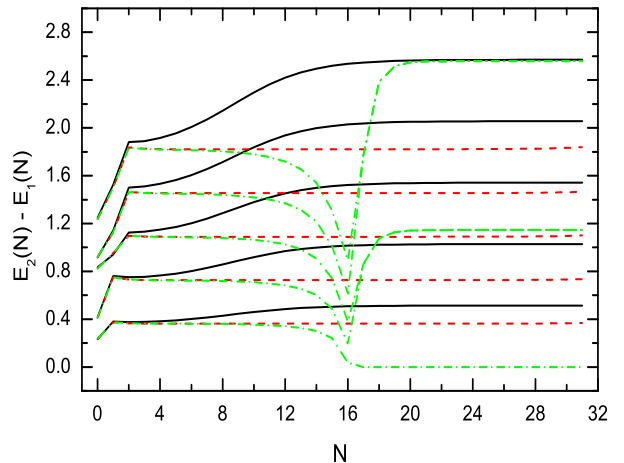


FIG. 3: NRG flow of excitation energies at $S = 0.3$, $\Delta = 0.0$ and $\epsilon = 0.1 > \epsilon_c$. The energy levels flow to three different fixed points: a stable free boson fixed point for $\alpha = 0.084 < \alpha_c^{(c)}$ (solid lines), an unstable critical fixed point for $\alpha = 0.08593945 \approx \alpha_c^{(c)}$ (dashed lines), and a strong-coupling fixed point for $\alpha = 0.086 > \alpha_c^{(c)}$ (dash-dotted lines). The NRG parameters are $\Lambda = 4.0$, $M_s = 100$, and $N_b = 8$.

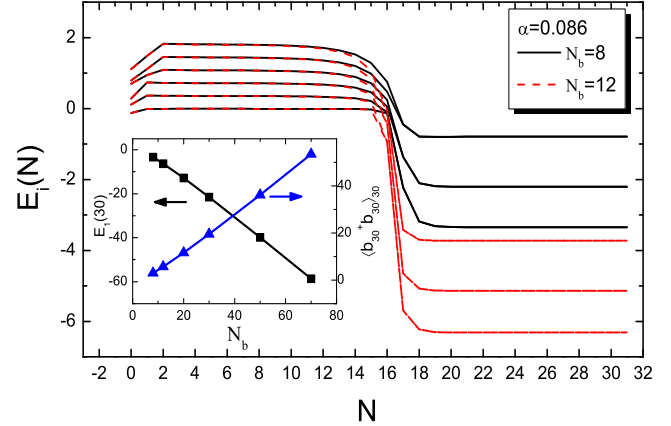


FIG. 4: NRG flow of $E_{i=1 \sim 6}(N)$ at $S = 0.3$, $\Delta = 0.0$, $\epsilon = 0.1 > \epsilon_c$, and $\alpha = 0.086 > \alpha_c^{(c)}$, obtained using $N_b = 8$ (solid lines) and $N_b = 12$ (dashed lines). Inset: ground state properties of the fixed point Hamiltonian $H_{N=30}$ as functions of N_b , the energy $E_1(30)$ (squares) and the boson occupancy number $\langle b_{30}^\dagger b_{30} \rangle_{N=30}$ (up triangles). The lines are for guiding eyes. Other NRG parameters are $\Lambda = 4.0$ and $M_s = 100$.

the ground state energy $E_1(N)$. While the energies for $N < 14$ is independent of N_b , the strong-coupling fixed point energies in $N > 16$ decreases with increasing N_b . As shown in the inset, both $E_1(N = 30)$ and the boson number $\langle b_{30}^\dagger b_{30} \rangle_{N=30}$ at the strong-coupling fixed point $N = 30$ are linear functions of N_b , diverging in the limit

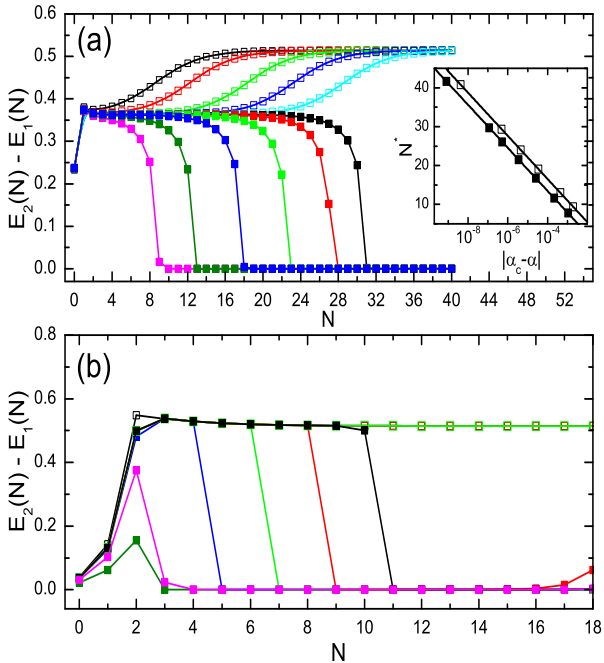


FIG. 5: Flow diagrams near the QPTs for $S = 0.3$ and $\Delta = 0.0$. (a) Continuous QPT for $\epsilon = 0.1 > \epsilon_c$, $\alpha_c^{(c)} \approx 0.08593448$, and (b) first-order QPT for $\epsilon = -0.2 < \epsilon_c$, $\alpha_c^{(1)} \approx 0.1014678$. From left to right, α increases for $\alpha < \alpha_c$ (empty squares) and α decreases for $\alpha > \alpha_c$ (solid squares). Lines are for guiding eyes. Inset of (a): power law fitting of $T^* = \Lambda^{-N^*} \propto |\alpha - \alpha_c|^{z\nu}$ for $\alpha < \alpha_c$ (empty squares) and $\alpha > \alpha_c$ (solid squares), giving $z\nu = 3.333$ and 3.338 , respectively. NRG parameters are $\Lambda = 4.0$, $M_s = 100$ and $N_b = 12$.

$N_b = \infty$. As a result, the total NRG ground state energy $E_{QSB} = \sum_{n=0}^{\infty} \Lambda^{-n} E_1(n)$ tends to minus infinity in the limit $N_b = \infty$. This supports that the strong-coupling fixed point is an unstable state of the environment.

To investigate the critical behaviour of the QPTs, the excitation energy flows are presented in Fig.5 for α very close to $\alpha_c^{(c)}$ and $\alpha_c^{(1)}$. In Fig.5(a), a typical critical behaviour is observed for $\epsilon = 0.1 > \epsilon_c$, with the standard scaling form. The crossover energy scale $T^* = \Lambda^{-N^*}$ is found to follow a power law, $T^* \propto |\alpha_c - \alpha|^{z\nu}$. The fitted exponent $z\nu = 3.333$ and $z\nu = 3.338$ from the two sides of $\alpha_c^{(c)}$ agree well with the exact solution $z\nu = 1/s$ at $s = 0.3$. In Fig.5(b), near the first-order phase transition at $\epsilon = -0.2 < \epsilon_c$, a level crossing in the energy flow is observed, accompanied with an abrupt jump from $S_z = 1/2$ to $S_z = -1/2$.

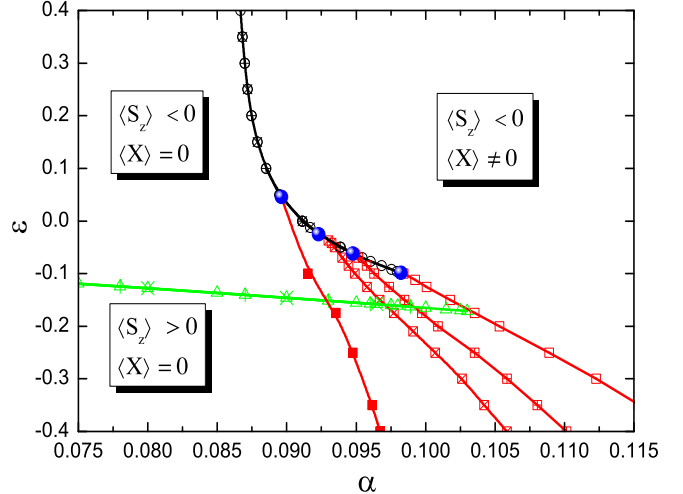


FIG. 6: Ground state phase diagram for $s = 0.3$ and $\Delta = 0.1$, obtained using $N_b = 12$ (empty symbols), $N_b = 20$ (plus-filled symbols), and $N_b = 30$ (cross-filled symbols). The continuous transition line, the first-order transition line, and the spin-flip line are marked by squares, circles, and up triangles, respectively. The solid dots are the jointing points of the first- and the continuous transitions. The first-order phase boundary is extrapolated to $N_b = \infty$ (solid squares) with the jointing point at $(\alpha_c = 0.0896, \epsilon_c = 0.0454)$. NRG parameters are $\Lambda = 4.0$, $M_s = 100$, $N_b = 12$.

B. Effects of finite quantum tunnelling $\Delta > 0$

1. the case of $s=0.3$

The quantum tunnelling $\Delta > 0$ introduces non-trivial dynamics of σ_z and modifies the phase diagram from the $\Delta = 0$ limit. Fig.6 shows the NRG phase diagram obtained for $s = 0.3$ and $\Delta = 0.1$. The boson-stable state ($\langle X \rangle = 0$) on the left side is separated from the boson-unstable phase ($\langle X \rangle \neq 0$) by a continuous or a first-order transition line, depending on the value of ϵ . The phase boundaries obtained using $N_b = 12, 20$, and 30 are presented as different squares. Same as the $\Delta = 0$ case, the continuous transition (circles) and the spin-flip line (up triangles) are almost independent of N_b , while the first-order transition line (squares) shifts to smaller α with increasing N_b , converging to an extrapolated line at $N_b = \infty$ (solid squares with eye-guiding line).

Several changes are induced by the finite quantum tunnelling. First, the phase boundaries has shifted quantitatively with respect to their position at $\Delta = 0$. The line of $\alpha_c^{(c)}$ is no longer vertical, especially near ϵ_c where the competition between ϵ and Δ is strong. For $\epsilon \gg \Delta$, $\alpha_c^{(c)}$ is independent of ϵ asymptotically. The jointing point ($\alpha_c = 0.08963, \epsilon_c = 0.04539$) of the continuous and the first-order QPT lines moves to larger ϵ direction, compared to $\Delta = 0$ case. Second, the spin-flip line is no longer accompanied with an abrupt jump of $\langle S_z \rangle$ between

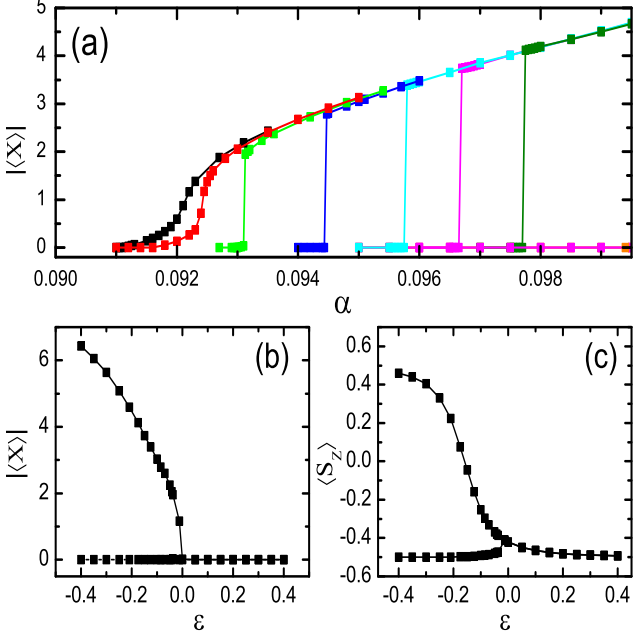


FIG. 7: $|\langle X \rangle|$ and $\langle S_z \rangle$ near the jointing point of the continuous and the first-order QPT, for $s = 0.3$ and $\Delta = 0.1$. (a) $|\langle X \rangle|(\alpha)$ for various ϵ 's. From left to right, $\epsilon = 0.0, -0.012, -0.037, -0.085, -0.125, -0.15$, and -0.175 . In (b) and (c), $|\langle X \rangle|$ and $\langle S_z \rangle$ values at the upper and lower edge of the transition are plotted as functions of ϵ . NRG parameters are $\Lambda = 4.0$, $M_s = 100$, $N_b = 30$.

$1/2$ and $-1/2$. As ϵ increases above ϵ_f for a given $\alpha < \alpha_c$, $\langle S_z \rangle$ changes smoothly from positive to negative values and no singularity is found in our NRG data. Therefore, the spin-flip line $\epsilon_f(\alpha)$ is not a phase transition line, due to the mixing of spin up and down subspaces by $\Delta > 0$. Finally, the spin-flip line $\epsilon_f(\alpha)$ ends on the first-order phase boundary $\alpha_c^{(1)}$, instead of ending at the tri-critical point as in the case of $\Delta = 0$. A small window of ϵ thus emerges below ϵ_c in which the first-order QPT is between the two states both with $\langle S_z \rangle < 0$. In contrast, for $\Delta = 0$ the first-order QPT is always between the $\langle S_z \rangle > 0$ and the $\langle S_z \rangle < 0$ states.

In Fig.7, we show how the QPT transits from first order into continuous as ϵ increases above ϵ_c . The evolution of the curves $\langle X \rangle(\alpha)$ with ϵ is shown in Fig.7(a). As shown in Fig.7(b) and (c), as ϵ approaches ϵ_c from below, the magnitude of the jumps in $\langle X \rangle$ and $\langle S_z \rangle$ at $\alpha_c^{(1)}$ decrease to zero, leading to a continuous QPT. Note that the spin is polarized on both sides of the QPT. Similar to the case $\Delta = 0$, NRG calculation shows that in the limit $N_b = \infty$, the boson-unstable phase has $|\langle X \rangle| = \infty$, regardless of the order of QPT.

Besides the change of phase diagram, a finite Δ also induces non-trivial $\sigma_z - \sigma_z$ dynamical correlation function. The coherence in the non-equilibrium evolution $\langle \sigma_z \rangle(t)$ can be partly reflected in the equilibrium dynamical cor-

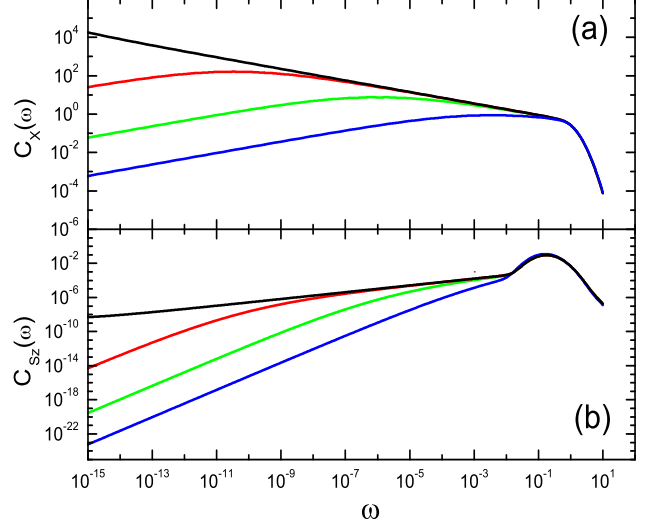


FIG. 8: Dynamical correlation functions (a) $C_X(\omega)$ and (b) $C_{Sz}(\omega)$ for $\alpha \leq \alpha_c^{(c)}$, calculate for $s = 0.3$, $\Delta = 0.1$, and $\epsilon = 0.0 > \epsilon_c$. From top to bottom, $\alpha = 0.091101 \approx \alpha_c^{(c)}$, 0.09105 , 0.09 , and 0.08 . The zero frequency peak $A\delta(\omega)$ of $C_{Sz}(\omega)$ is not shown. NRG parameters are $\Lambda = 4.0$, $M_s = 100$, $N_b = 12$. The broadening parameter $B = 1.0$.

relation function

$$C_{Sz}(\omega) = \frac{1}{2\pi} \int_{-\infty}^{+\infty} C_{Sz}(t) e^{i\omega t} dt \quad (18)$$

with $C_{Sz}(t) \equiv (1/2)\langle \{S_z(t), S_z(0)\} \rangle$. At $T = 0$, $C_{Sz}(\omega) = C_{Sz}(-\omega)$ and it fulfills the sum rule $\int_{-\infty}^{\infty} C_{Sz}(\omega) d\omega = 1/4$. For a non-degenerate ground state $|G\rangle$, $C_{Sz}(\omega) = A\delta(\omega) + C'_{Sz}(\omega)$, where $A = \langle G|S_z|G\rangle^2/2$. At $\Delta = 0$, there is no dynamics in the S_z component and $C_{Sz}(\omega) = \delta(\omega)/4$. For $\Delta > 0$, the spin is no longer fully polarized in z -direction and the weight of $C_{Sz}(\omega)$ is partially transferred from $\omega = 0$ to $\omega > 0$ regime.

In Fig.8(a) and (b), $C_X(\omega)$ and $C_{Sz}(\omega)$ are presented for $\epsilon = 0.0 > \epsilon_c$ and $\alpha \leq \alpha_c^{(c)}$. In Fig.8(a), the low frequency asymptotic behaviour of $C_X(\omega)$ is shown to be the same as the $\Delta = 0$ case, *i.e.*, $C_X(\omega) \propto \omega^s$ and $\propto \omega^{-s}$ for $\omega \ll \omega^*$ and $\omega \gg \omega^*$, respectively. ω^* approaches zero as $\omega^* \propto (\alpha_c^{(c)} - \alpha)^{1/s}$. In Fig.8(b), $C_{Sz}(\omega)$ is found to be characterized by a coherent peak around the effective Rabi frequency $\omega = \omega_R$ and a low frequency power law behaviour, $C_{Sz}(\omega) \propto \omega^{\theta_f}$ for $\alpha < \alpha_c$ and $C_{Sz}(\omega) \propto \omega^{\theta_c}$ at $\alpha = \alpha_c^{(c)}$. For $\alpha < \alpha_c^{(c)}$, the same crossover scale ω^* as in $C_X(\omega)$ separates the ω^{θ_0} (for $\omega < \omega^*$) and ω^{θ_c} (for $\omega > \omega^*$) behaviour. A zero frequency peak $A\delta(\omega)$ is also present but not shown. Our NRG data for the sub-Ohmic regime $0 < s < 1$ support $\theta_0 = 1 + 2s$ and $\theta_c = 1 - 2s$ (see Fig.10), being independent of ϵ and Δ values. In contrast, the linear-coupling SBM has $\theta_0 = s$ and $\theta_c = -s$. Here, the effect of the quadratic impurity-bath coupling is prominent: the existence of impurity

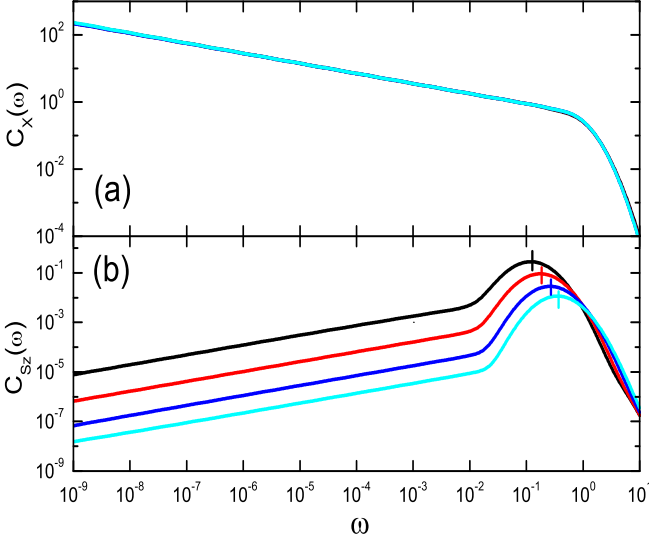


FIG. 9: Dynamical correlation functions (a) $C_X(\omega)$ and (b) $C_{Sz}(\omega)$ for $\epsilon > \epsilon_c \approx -0.098$, calculated at $s = 0.3$, $\Delta = 0.1$ and $\alpha = \alpha_c^{(c)}(\epsilon)$. From top to bottom, $\epsilon = -0.085, 0.0, 0.1$, and 0.2 . The corresponding $\langle S_z \rangle$ values are $-0.310, -0.421, -0.465$, and -0.481 . The zero frequency peak $A\delta(\omega)$ is not shown. In (b), the vertical dashes mark the Rabi frequency ω_R estimated from $\langle S_z \rangle$. NRG parameters are $\Lambda = 4.0$, $M_s = 100$, $N_b = 12$. The broadening parameter $B = 1.0$.

influences the bath spectral function and it subsequently modifies the dynamics of the impurity itself.

Close to the first-order QPT at $\epsilon < \epsilon_c$ and $\alpha \leq \alpha_c^{(1)}$, $C_X(\omega)$ and $C_{Sz}(\omega)$ are similar to the ones at $\epsilon > \epsilon_c$ and $\alpha < \alpha_c^{(c)}$. At $\alpha = \alpha_c^{(1)}$, both correlation functions change abruptly into an artefact produced by the finite N_b used in NRG. In the $\Delta = 0$ case, the critical behaviour cannot be observed in $\epsilon < \epsilon_c$ and $\alpha < \alpha_c^{(1)}$ regime, because the lower subspace $\sigma_z = +1$ has no QPT. For $\Delta > 0$, due to the mixing of two subspaces, quantum critical behaviour such as $C_X(\omega) \propto \omega^{-s}$ and $C_{Sz}(\omega) \propto \omega^{1-2s}$ can be observed in the intermediate frequency regime $\omega^* \ll \omega \ll \Omega_R$ for the weak first-order QPT in $\epsilon \lesssim \epsilon_c$ and $\alpha \lesssim \alpha_c^{(1)}$ regime. The crossover scale ω^* decreases with increasing α and reaches a finite value at the first-order QPT $\alpha = \alpha_c^{(1)}$. As ϵ approaches ϵ_c from below, $\omega^*(\alpha = \alpha_c^{(1)})$ decreases to zero and the first order QPT transits into continuous one.

Fig.9 shows the dynamical correlation functions $C_X(\omega)$ and $C_{Sz}(\omega)$ at the critical point $\alpha = \alpha_c^{(c)}$ for a series of ϵ in the regime $\epsilon > \epsilon_c$. Although $C_X(\omega)$ is identical for different ϵ values, $C_{Sz}(\omega)$ decreases with increasing ϵ and keeps the exponent $\theta_c = 1 - 2s$ intact. This is because as ϵ increases, $\langle S_z \rangle(\alpha = \alpha_c^{(c)})$ decrease monotonically to $-1/2$, transferring the weight of $C_{Sz}(\omega)$ from the $\omega > 0$ regime to $\omega = 0$. The prominent Rabi

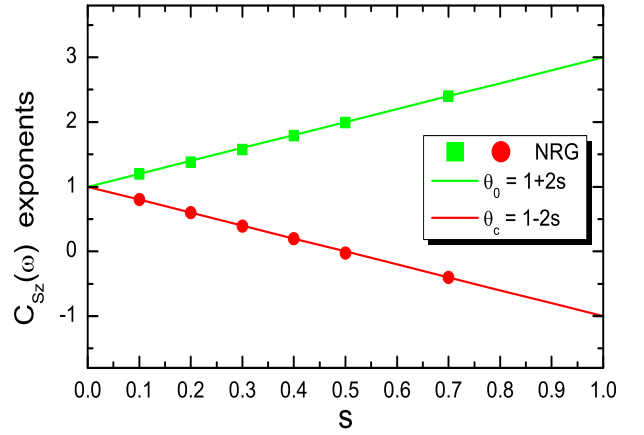


FIG. 10: Exponents of $C_{Sz}(\omega)$: η_0 and η_c . The solid lines are $\eta_0 = 1 + 2s$ and $\eta_c = 1 - 2s$.

peak corresponds to short-time coherent oscillations in the population $P(t) = \langle S_z(t) \rangle$ of the non-equilibrium situation. The effective Rabi frequency ω_R increases with ϵ . Assuming an effective free spin Hamiltonian, we can write $\omega_R = \sqrt{\epsilon_{eff} + \Delta_r}$ where ϵ_{eff} contains both ϵ and the static mean field from the quadratic coupling $(g_2/2)\sigma_z Y^2$. Δ_r is the renormalized tunnelling strength. The estimated ω_R by assuming $\Delta_r \approx \Delta$ and using $\langle S_z \rangle$ from NRG agrees well with the peak position in $C_{Sz}(\omega)$ (vertical dashes in Fig.9). This shows that robust coherent spin evolution persists to the strongest coupling allowed before the environmental QPT occurs.

2. other s values

We carried out NRG study for other s values and confirmed that the scenario of QPT established at $s = 0.3$ applies to the whole sub-Ohmic regime $0 \leq s < 1$, with important quantitative differences. For $\Delta = 0$, the structure of the phase diagram is same as that of $s = 0.3$ and NRG results agree well with the exact solution. For $\Delta > 0$, we find that ϵ_c increases with s and the first-order QPT line expands to larger ϵ values. At $T = 0$, the critical fluctuation of \hat{X}

$$\langle X^2 \rangle = 2 \int_0^\infty C_X(\omega) d\omega \propto \int_0^\infty \omega^{-s} d\omega \quad (19)$$

increases with s . For larger s , the ground state energy contains a term $\langle \sigma_z X^2 \rangle$ which changes more rapidly with the flipping of spin. This makes the continuous QPT more difficult to realize. Our NRG study for $s = 0.7$ supports that $\alpha_c = \infty$ for any finite Δ , *i.e.*, the transition is first-order for any $\Delta > 0$ and any ϵ . This behaviour is well understood at the extreme case $s \geq 1$ where the infra-red divergence in $\langle X^2 \rangle$ makes the continuous QPT

impossible. Here, the continuous versus first-order phase transition is an interesting problem on its own, giving its resemblance to the same problem in the crystal lattice [47]. A detailed study on this issue will be published elsewhere. At the other limit $s = 0$ which is related to the $1/f$ noise in the quantum circuit, a finite Δ induces a small but finite $\alpha_c^{(c)}$. $z\nu = 1/s$ diverges at $s = 0$ and a QPT of the Kosterlitz-Thouless type occurs, as confirmed by the NRG calculation (not shown). This is similar to the situation of linear-coupling SBM [13].

The above analysis also explains the observation that for larger s , reliable NRG calculations require larger N_b and are hence more difficult. For studying the continuous QPT at $\epsilon > \epsilon_c$, insufficient N_b could lead to artificial critical fixed point and produce incorrect exponents $z\nu$, θ_0 and θ_c . For studying the first-order QPT at $\epsilon < \epsilon_c$, it may make an artificial continuous QPT. Up to now, quantitatively accurate study of $H_{QSB}(\Delta > 0)$ for $s > 1$ is still a technical challenge for NRG. For the sub-Ohmic bath, however, we can get reliable results using the boson number truncation up to $N_b = 50$ and a large logarithmic discretization parameter $\Lambda = 10.0$. For $s \lesssim 1$ where the first-order QPT prevails, the critical exponents can still be extracted reliably from the intermediate frequency regime $\omega^* \ll \omega \ll \omega_R$ for $\epsilon \lesssim \epsilon_c$ and $\alpha \lesssim \alpha_c^{(1)}$.

In Fig.10, we show the exponents θ_0 and θ_c of $C_{Sz}(\omega)$. They are defined as $C_{Sz}(\omega) \propto \omega^{\theta_0}$ for $\omega \ll \omega^*$ and $C_{Sz}(\omega) \propto \omega^{\theta_c}$ for $\omega \gg \omega^*$, with the same crossover scale ω^* of $C_X(\omega)$. Since they appear only at $\Delta > 0$, there is no exact solution for them. The NRG data agree with the analytical expressions $\theta_0 = 1 - 2s$ and $\theta_c = 1 + 2s$ within an error of 2%. When extended to $s \geq 1$, such behaviour will lead to the breakdown of the sum rule of $C_{Sz}(\omega)$ and prohibit the continuous QPT in the Ohmic- and super-Ohmic regime.

IV. DISCUSSION AND SUMMARY

In this section, we discuss several issues regarding to the impurity-induced environmental QPT that we studied in this paper.

First, we note that the unphysical result $\langle X \rangle = \pm\infty$ and $E_g = -\infty$ in the boson-unstable state is a consequence of incompleteness of the present model. Whenever such QPT occurs in a realistic situation, the magnitude of boson displacement is confined by the higher order anharmonic terms of the boson energy beyond H_{QSB} , leading to a local environmental distortion with finite $\langle X \rangle$ as a new stable state. Such higher order terms will determine the properties of the new stable state of the environment but cannot remove the impurity-induced environmental QPT. The environmental instability shows up differently in real systems. For the superconducting flux qubit system [31], $\langle X \rangle \neq 0$ corresponds to an additional bias current in the SQUID oscillator. In the experiment of quantum dot system [41, 42], however, the boson instability corresponds to a local distortion of the

crystal lattice. In the optical spectra signal of an impurity center in crystals, the instability is detected by the anomalous temperature dependence of the zero-phonon line width due to the softening of bosonic modes close to the environmental QPT [48]. In the NRG calculation, the boson state truncation N_b mimics such a higher order anharmonic effect accidentally. We find that although the existence of the QPT is robust under this constraint of Hilbert space, the critical exponents $z\nu$ and θ_c may well be changed by it.

Second, we discuss the situation where both the linear- and the quadratic-coupling are present. In that case, the Hamiltonian reads

$$H_{SB} = \frac{\epsilon}{2}\sigma_z - \frac{\Delta}{2}\sigma_x + \sum_i \omega_i a_i^\dagger a_i + \frac{g_1}{2}\sigma_z \hat{Y} + \frac{g_2}{2}\sigma_z \hat{Y}^2. \quad (20)$$

For general parameters $g_1 \neq 0$ and $g_2 \neq 0$, this Hamiltonian has a lower symmetry than both the linear-coupling SBM and the pure quadratic-coupling one. As a result, neither the delocalize-localize transition nor the environmental stable-unstable transition exists any more. Instead, similar to the situation of linear-coupling SBM under a finite bias ϵ , it is expect that the ground state smoothly interpolates between different limiting symmetry-broken states of purely linear- or quadratic-coupling Hamiltonians. The crossover lines separating these phases are determined by the relative strength of g_1 , g_2 , and the crossover energy scale T^* to the quantum critical regimes in g_1 - and g_2 -only cases [49, 50]. However, both the bath and the spin dynamics will be severely influenced by the existence of the quadratic coupling terms.

At finite temperatures, the QPT observed in H_{QSB} no longer exists. However, for parameters close to the critical point and $\Delta > 0$, the quantum critical properties will appear in the temperatures regime $T > T^*$, as demonstrated in the proposal of observing the impurity QPT in a mesoscopic metal ring system [26]. This provides opportunities to experimentally observe the signatures of the environmental QPT discussed in this paper. Our conclusion about the environmental QPT can be straightforwardly extended to the single boson mode case. For the Hamiltonian of the circuit quantum electrodynamics $H = \omega_p a^\dagger a + (\Delta/2)\sigma_x + (\epsilon/2)\sigma_z + g_2(a^\dagger + a)^2\sigma_z$ [31], the boson-instability occurs at $g_2/\omega_p > 1/4$ for $\Delta = 0$. Using the parameters of the experimental set up of Ref. [31], we estimate that $g_2 \sim 5.0$ MHz. Given $\omega_p = 3.17$ GHz, the actual ratio $g_2/\omega_p \sim 10^{-3}$, much smaller the critical value. However, in the experiments of superconducting qubit, methods are available to both engineer the shape of $J(\omega)$ [51] for low frequency continuous environment, and to enhance the spin-boson coupling to the ultra-strong regime for the case of discrete boson modes [52–54]. Especially, the new technique of switchable coupling can boost the linear coupling from 10^2 MHz level to GHz level, making it comparable to ω_p [55]. The superconducting flux qubit [33, 34] or the quantum dot [35] under the $1/f$ noise can also be tuned to the optimal

working point. Considering that our results predict that the $1/f$ noise with quadratic spin-boson coupling gives a much smaller α_c , we expect that these advances can make it feasible to detect the environmental QPT discussed in this work.

In summary, the quadratic-coupling spin-boson model is found to have an impurity-induced environmental QPT between the boson-stable and -unstable ground states. Using the exact solution at $\Delta = 0$ as well as the NRG calculation, we establish the ground state phase diagram which contains both continuous and first-order QPTs. The exact quantum critical behaviour is obtained. The non-trivial features of the spin as well as the bath dynamical correlation functions are revealed. Our results are relevant to various recent experimental set ups, including the superconducting flux qubit at the optimal working point [30–32], the quantum dot quadratically coupled to acoustic phonons [42], and the impurity atom embedded in a crystal [48]. The physical consequence of such QPTs and the feasibility of its experimental observation are discussed.

V. ACKNOWLEDGEMENTS

D.-C. Zheng and N.-H. Tong acknowledge helpful discussions with Y.-J. Yan. This work is supported by 973 Program of China (2012CB921704), NSFC grant (11374362), Fundamental Research Funds for the Central Universities, and the Research Funds of Renmin University of China 15XNLQ03.

Appendix A: Exact solution at $\Delta = 0$

In this appendix, we derive the exact solution at $\Delta = 0$. The Hamiltonian H_{QSB} at $\Delta = 0$ reads

$$H_{QSB}(\Delta = 0) = \frac{\epsilon}{2}\sigma_z + \sum_i \omega_i a_i^\dagger a_i + \frac{g_2 \eta_0}{2\pi} \sigma_z \hat{X}^2. \quad (\text{A1})$$

Here $X = b_0 + b_0^\dagger$ and $b_0 = \sqrt{\pi/\eta_0} \sum_i \lambda_i a_i$. For the spectral function $J(\omega)$ specified in Eq.(4), $\eta_0 \equiv \pi \sum_i \lambda_i^2 = 2\pi\alpha\omega_c^2/(1+s)$.

To solve $H_{QSB}(\Delta = 0)$ exactly, we employ the equation of motion (EOM) for the double-time Green's function $\langle\langle X|X \rangle\rangle_\omega$. At zero temperature $T = 0$, the dynamical correlation function $C_X(\omega)$ is expressed in terms of $\langle\langle X|X \rangle\rangle_\omega$ as

$$C_X(\omega) = -\frac{1}{2\pi} \text{Sgn}(\omega) \text{Im} \langle\langle X|X \rangle\rangle_{\omega+i\eta} \quad (\text{A2})$$

Here $\eta = 0^+$ is an infinitesimal positive number. Note that $C_X(\omega)$ is an even function of ω .

We start from the EOM of the following GF component,

$$\omega \langle\langle a_i | X \rangle\rangle_\omega = \langle [a_i, X] \rangle + \langle\langle [a_i, H_{QSB}] | X \rangle\rangle_\omega. \quad (\text{A3})$$

At $\Delta = 0$, the commutators in the above equation read $[a_i, X] = \sqrt{\pi/\eta_0} \lambda_i$, $[a_i, H_{QSB}] = \omega_i a_i + g_2 \lambda_i \sigma_z \sum_l \lambda_l (a_l + a_l^\dagger)$. Using these expressions and their Hermitian conjugates, we obtain

$$\omega \langle\langle a_i + a_i^\dagger | X \rangle\rangle_\omega = \omega_i \langle\langle a_i - a_i^\dagger | X \rangle\rangle_\omega \quad (\text{A4})$$

and

$$\begin{aligned} \omega \langle\langle a_i - a_i^\dagger | X \rangle\rangle_\omega &= 2\sqrt{\pi/\eta_0} \lambda_i + \omega_i \langle\langle a_i + a_i^\dagger | X \rangle\rangle_\omega \\ &+ 2g_2 \sqrt{\eta_0/\pi} \sigma_z \lambda_i \langle\langle X | X \rangle\rangle_\omega. \end{aligned} \quad (\text{A5})$$

One can solve Eq.(A4) and (A5) to obtain

$$\begin{aligned} \langle\langle a_i + a_i^\dagger | X \rangle\rangle_\omega &= \sqrt{\frac{\pi}{\eta_0}} \frac{2\lambda_i \omega_i}{\omega^2 - \omega_i^2} \\ &+ g_2 \sqrt{\frac{\pi}{\eta_0}} \frac{2\lambda_i \omega_i}{\omega^2 - \omega_i^2} \sigma_z \langle\langle X | X \rangle\rangle_\omega. \end{aligned} \quad (\text{A6})$$

Multiplying λ_i on both sides of the above equation and summing over i , we obtain a closed equation for $\langle\langle X | X \rangle\rangle_\omega$. The solution of the equation reads

$$\langle\langle X | X \rangle\rangle_\omega = \frac{2\pi/\eta_0 \sum_i \frac{\lambda_i^2 \omega_i}{\omega^2 - \omega_i^2}}{1 - 2g_2 \sigma_z \sum_i \frac{\lambda_i^2 \omega_i}{\omega^2 - \omega_i^2}}. \quad (\text{A7})$$

Using $g(\omega)$ defined in Eq.(10) of the main text, it is expressed as

$$\langle\langle X | X \rangle\rangle_\omega = \frac{g(\omega) + g(-\omega)}{1 - \frac{g_2 \eta_0}{\pi} \sigma_z [g(\omega) + g(-\omega)]}. \quad (\text{A8})$$

Carrying out the analytical continuation $\omega \rightarrow \omega + i\eta$ and taking the imaginary part, we obtain the exact expression for $C_X(\omega)$ in Eq.(9) of the main text. $g(\omega)$ can be simplified as

$$\begin{aligned} g(\omega) &\equiv \frac{1}{\eta_0} \mathcal{P} \int_0^\infty \frac{J(\epsilon)}{\omega - \epsilon} d\epsilon \\ &= \frac{1+s}{\omega_c} \mathcal{P} \int_0^1 \frac{x^s}{\omega/\omega_c - x} dx, \end{aligned} \quad (\text{A9})$$

and finally we obtain [56]

$$g(\omega) = \frac{1}{\omega} F(1, 1+s; 2+s; \frac{\omega_c}{\omega}). \quad (\text{A10})$$

Here $F(\alpha, \beta; \gamma; z)$ is the hypergeometric function. For the numerical calculation in $0 < \omega < \omega_c$ and the analysis of $C_X(\omega = 0)$, the above expression is transformed by analytical continuation into (for $\omega > 0$)

$$\begin{aligned} g(\omega) &= -\frac{1}{\omega_c} \frac{1+s}{s} F(1, -s; 1-s; \omega/\omega_c) \\ &+ \frac{\omega^s}{\omega_c^{1+s}} \cos[\pi(1+s)] \Gamma(2+s) \Gamma(-s), \end{aligned} \quad (\text{A11})$$

and

$$g(-\omega) = -\frac{1}{\omega_c} \frac{1+s}{s} F(1, -s; 1-s; -\omega/\omega_c) - \frac{\omega^s}{\omega_c^{1+s}} \Gamma(2+s) \Gamma(-s). \quad (\text{A12})$$

Here $\Gamma(z)$ is the Gamma function. Series expansions can then be used for numerical evaluations, $F(1, -s; 1-s; z) = -\sum_0^\infty [s/(n-s)] z^n$ for $0 \leq z < 1$ [56]. Note that the analytical continuation does not apply to integer values of $s = 0, 1, 2, \dots$

In order to calculate $E_g^{(+1)}$ and $E_g^{(-1)}$, we start from the expression at $\Delta = 0$

$$E_g^{\sigma_z} = \frac{\epsilon}{2} \sigma_z + \frac{g_2 \eta_0}{2\pi} \sigma_z \langle X^2 \rangle + \sum_i \omega_i \langle a_i^\dagger a_i \rangle. \quad (\text{A13})$$

The energy difference is

$$\begin{aligned} \delta E_g &\equiv E_g^{(+1)} - E_g^{(-1)} \\ &= \epsilon + \frac{g_2 \eta_0}{2\pi} \left[\langle X^2 \rangle^{(+1)} + \langle X^2 \rangle^{(-1)} \right] \\ &\quad + \sum_i \omega_i \left[\langle a_i^\dagger a_i \rangle^{(+1)} - \langle a_i^\dagger a_i \rangle^{(-1)} \right]. \end{aligned} \quad (\text{A14})$$

The averages can be calculated from corresponding GFs using the dissipation-fluctuation theorem. For this purpose, besides $\langle \langle X | X \rangle \rangle_\omega$ obtained above, we still need $\langle \langle a_i | a_i^\dagger \rangle \rangle_\omega^{\sigma_z}$ which is obtained as

$$\langle \langle a_i | a_i^\dagger \rangle \rangle_\omega^{\sigma_z} = \frac{1}{\omega - \omega_i} + \frac{\lambda_i^2}{(\omega - \omega_i)^2} \left[g_2 \sigma_z + g_2^2 \frac{\eta_0}{\pi} \langle \langle X | X \rangle \rangle_\omega \right]. \quad (\text{A15})$$

The fluctuation-dissipation theorem at $T = 0$ gives

$$\delta E_g = \epsilon + \frac{1}{\pi} \int_{-\infty}^0 \text{Im} H_{\omega+i\eta} d\omega, \quad (\text{A16})$$

with

$$\begin{aligned} H_\omega &= \frac{g_2 \eta_0}{2\pi} \left[\langle \langle X | X \rangle \rangle_\omega^{(+1)} + \langle \langle X | X \rangle \rangle_\omega^{(-1)} \right] \\ &\quad + \sum_i \omega_i \left[\langle \langle a_i | a_i^\dagger \rangle \rangle_\omega^{(+1)} - \langle \langle a_i | a_i^\dagger \rangle \rangle_\omega^{(-1)} \right]. \end{aligned} \quad (\text{A17})$$

Inserting Eq.(A8) and (A15) into this expression, we obtain the results Eqs.(14)-(16) of the main text. Using the $J(\omega)$ in Eq.(4) and Taylor expanding Eq.(A16), we obtain

$$\begin{aligned} \delta E_g &= \epsilon + \frac{g_2}{\pi} \int_{-\omega_c}^0 J(-\omega) d\omega + \mathcal{O}(\alpha^3) \\ &= \epsilon + \frac{2\alpha}{1+s} (g_2 \omega_c^2) + \mathcal{O}(\alpha^3). \end{aligned} \quad (\text{A18})$$

The approximate spin-flip line Eq.(17) is obtained as the solution to $\delta E_g = 0$.

Appendix B: NRG Formalism for H_{QSB}

In this appendix, we summarize the bosonic NRG formalism used to study H_{QSB} . Following the logarithmic discretization method of Bulla [57], the Hamiltonian of the quadratic-coupling SBM can be mapped into the star-type Hamiltonian

$$H_{\text{star}} = \frac{\epsilon}{2} \sigma_z - \frac{\Delta}{2} \sigma_x + \frac{g_2}{2} \sigma_z \hat{Y}^2 + \sum_{n=0}^{\infty} \xi_n a_n^\dagger a_n. \quad (\text{B1})$$

The local boson displacement operator \hat{Y} is expressed as $\hat{Y} = \sum_{n=0}^{\infty} (\gamma_n / \sqrt{\pi}) (a_n^\dagger + a_n)$. The coefficients ξ_n and γ_n reads

$$\xi_n = \frac{\int_{\Lambda-(n+1)\omega_c}^{\Lambda^{-n}\omega_c} \omega J(\omega) d\omega}{\int_{\Lambda-(n+1)\omega_c}^{\Lambda^{-n}\omega_c} J(\omega) d\omega}, \quad (\text{B2})$$

and

$$\gamma_n = \left[\int_{\Lambda-(n+1)\omega_c}^{\Lambda^{-n}\omega_c} J(\omega) d\omega \right]^{1/2}. \quad (\text{B3})$$

Carrying out an orthogonal transformation for the boson modes, one obtains the Wilson-chain Hamiltonian

$$\begin{aligned} H_{\text{chain}} &= \frac{\epsilon}{2} \sigma_z - \frac{\Delta}{2} \sigma_x + \frac{g_2}{2} \sigma_z \hat{Y}^2 \\ &\quad + \sum_{n=0}^{\infty} \left[t_n \left(b_n^\dagger b_{n+1} + b_{n+1}^\dagger b_n \right) + \epsilon_n b_n^\dagger b_n \right]. \end{aligned} \quad (\text{B4})$$

Here $\hat{Y} = \sqrt{\eta_0/\pi} (b_0^\dagger + b_0)$. The coefficients t_n and ϵ_n are expressed by the following recursive formula ($m \geq 0$)

$$t_m = \left[\sum_{n=0}^{+\infty} \left[(\xi_n - \epsilon_m) u_{mn} - t_{m-1} u_{m-1n} \right]^2 \right]^{1/2}, \quad (\text{B5})$$

$$u_{m+1n} = \frac{1}{t_m} \left[(\xi_n - \epsilon_m) u_{mn} - t_{m-1} u_{m-1n} \right], \quad (\text{B6})$$

and

$$\epsilon_m = \sum_{n=0}^{+\infty} \xi_n u_{mn}^2. \quad (\text{B7})$$

The initial condition for the recursive calculation is $t_{-1} = 0$, $u_{-1n} = 0$, $u_{0n} = \gamma_n / \sqrt{\eta_0}$ with $\eta_0 = \sum_{n=0}^{+\infty} \gamma_n^2$.

The RG transformation is established for $N \geq 0$

$$\begin{aligned} H_{N+1} &= \Lambda H_N \\ &\quad + \Lambda^{N+1} \left[t_N \left(b_N^\dagger b_{N+1} + b_{N+1}^\dagger b_N \right) + \epsilon_{N+1} b_{N+1}^\dagger b_{N+1} \right], \end{aligned} \quad (\text{B8})$$

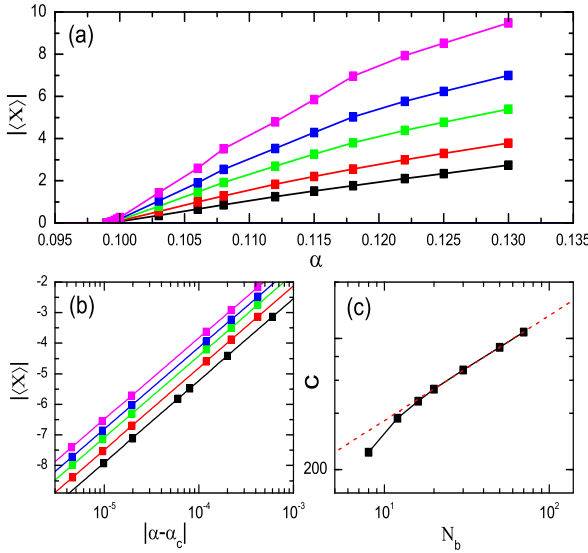


FIG. 11: The critical behaviour of the order parameter $|\langle X \rangle|$ near the continuous QPT $\alpha = \alpha_c^{(c)}$, for $S = 0.3$, $\Delta = 0.0$, and $\epsilon = 0.1 > \epsilon_c$. (a) $|\langle X \rangle|(\alpha)$ curves for different N_b values. From bottom to top, $N_b = 8, 12, 20, 30, 50$. (b) Power law fitting of $|\langle X \rangle| = c(\alpha - \alpha_c)^{\beta}$ with the fitted value $\beta = 1.16$. (c) Log-log plot of the pre-factor c versus N_b . The dashed line gives the fitting $c(N_b) \propto N_b^{0.56}$ in the large N_b limit. The NRG parameters are $\Lambda = 9.0$, $M_s = 100$.

with the starting Hamiltonian H_0

$$H_0 = \frac{\epsilon}{2} \sigma_z - \frac{\Delta}{2} \sigma_x + \epsilon_0 b_0^\dagger b_0 + \frac{1}{2} g_2 \sigma_z \hat{Y}^2. \quad (\text{B9})$$

The chain Hamiltonian is recovered in the limit of $N = \infty$ as $H_{\text{chain}} = \lim_{N \rightarrow \infty} \Lambda^{-N} H_N$. The above NRG formalism is the same as that for the liner-coupling SBM, except that we replaced \hat{Y} in the linear-coupling term with \hat{Y}^2 [14].

Appendix C: Quantitative Comparison of NRG and exact solution at $\Delta = 0$

In this Appendix, we make quantitative comparison between NRG results and the exact solution at $\Delta = 0$, for the order parameter $\langle X \rangle$, the phase boundaries, dynamical correlation function $C_X(\omega)$, and the exponents $z\nu$, y_0 , and y_c . For this purpose, we extrapolate NRG data to the limit $\Lambda = 1.0$, $M_s = \infty$ and $N_b = \infty$.

Fig.11 shows the extrapolation of the order parameter $\langle X \rangle$, together with its critical behaviour at $\alpha = \alpha_c^{(c)}$, to the limit $N_b = \infty$ for $s = 0.3$ and $\epsilon = 0.1 > \epsilon_c$. We used a large $\Lambda = 10$ and the data are found to be stable with the increase of M_s . Due to the truncation of the local boson Hilbert space, NRG always produces a finite $|\langle X \rangle|$ which increases with N_b , as shown in Fig.11(a). In Fig.11(b),

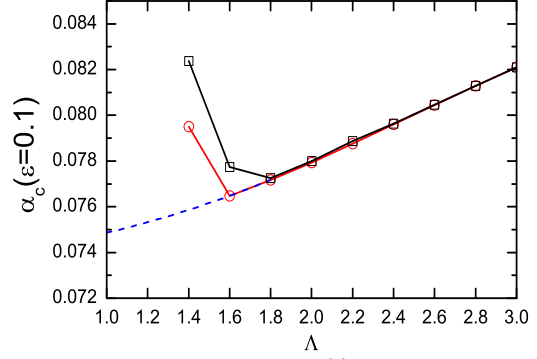


FIG. 12: Extrapolation of $\alpha_c^{(c)}$ to the limit $\Lambda = 1.0$ for $S = 0.3$, $\Delta = 0.0$, and $\epsilon = 0.1 > \epsilon_c$. The squares and circles represent data obtained using $M_s = 100$ and $M_s = 200$, respectively, with $N_b = 12$. The 4-point Lagrangian extrapolation using $\Lambda = 1.6, 1.8, 2.0$, and 2.2 gives the dashed line and the extrapolated value $\alpha_c(\Lambda = 1) = 0.07487$, in good agreement with the exact result $\alpha_c = s/(4g_2\omega_c)$.

the critical behaviour $|\langle X \rangle| \propto c(\alpha - \alpha_c)^{\beta}$ is shown to exist under the N_b -constraint, with the critical exponent $\beta = 1.16$ for $s = 0.3$. For general $0 < s < 1$ we find that β agrees well with the expression $\beta = (1 - s)/(2s)$. In the mean-field analysis of the linear-coupling SBM, this expression is a result from the boson-state truncation [58, 59]. With increasing N_b , β keeps unchanged and the pre-factor c increases as $c(N_b) \propto N_b^{0.56}$ as shown in Fig.11(c), signalling the divergence of $|\langle X \rangle|(\alpha > \alpha_c^{(c)})$ at $N_b = \infty$. For the parameter used here, $\alpha_c^{(c)} = 0.09918$ does not change either with N_b or with M_s .

In Fig.12, we extrapolate the NRG result for the continuos QPT point $\alpha_c^{(c)}$ at $\epsilon = 0.1 > \epsilon_c$ to $\Lambda = 1.0$. With larger M_s , $\alpha_c^{(c)}$ can be calculated reliably at smaller Λ . The 4-point Lagrangian extrapolation using $\Lambda = 1.6, 1.8, 2.0$, and 2.2 gives $\alpha_c^{(c)}(\Lambda = 1.0) = 0.0749$, very close to the exact result $\alpha_c^{exc} = s/(4g_2\omega_c) = 0.075$ for $s = 0.3$. For each Λ , we used the data from sufficiently large $M_s = 200$ and $N_b = 12$. For $\Delta = 0$, $\alpha_c^{(c)}$ from NRG is independent of ϵ in the regime $\epsilon > \epsilon_c$.

The extrapolation of the first-order QPT point $\alpha_c^{(1)}$ to $N_b = \infty$ is demonstrated in Fig.13, for $s = 0.3$ and at the bias $\epsilon = -0.2 < \epsilon_c$. In Fig.13(a), $|\langle X \rangle|$'s are plotted as functions of α (empty circles with eye-guiding lines). For each N_b , at $\alpha = \alpha_c^{(1)}$ the curve jumps from zero to a finite value which is on the curve of $\epsilon = 0.1$, for which a continuous QPT occurs at $\alpha_c^{(c)} = 0.09918$. With increasing N_b , $|\langle X \rangle|$ increases and $\alpha_c^{(1)}$ moves towards $\alpha_c^{(c)}$. Fig.13(b) shows that the distance $|\alpha_c^{(1)} - \alpha_c^{(c)}| \propto N_b^{-0.4}$, proving that $\alpha_c^{(1)} = \alpha_c^{(c)}$ in the limit $N_b = \infty$. This agrees with the exact solution. $|\langle X \rangle_c^{(1)}|$ shown in Fig.13(c) is the value at the upper edge of the the jump $\alpha = \alpha_c^{(1)} + 0^+$. It also diverges in the limit $N_b = \infty$, as

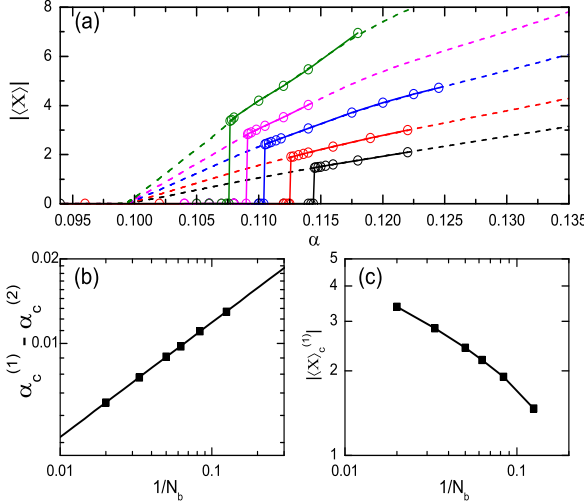


FIG. 13: The curves $|\langle X \rangle|(\alpha)$ near the first-order QPT for $S = 0.3$, $\Delta = 0.0$, and $\epsilon = -0.2 < \epsilon_c$. In (a), the empty circles with eye-guiding lines are NRG data using various N_b 's. From bottom to top, $N_b = 8, 12, 20, 30, 50$. The dashed lines are corresponding data for $\epsilon = 0.1 > \epsilon_c$. (b) Distance of the first-order QPT point $\alpha_c^{(1)}$ to the continuous one $\alpha_c^{(c)}$ as a function of $1/N_b$. The solid squares are NRG data and the solid line is a power law fit with the slope -0.4 . (c) $|\langle X \rangle|$ value at the upper edge of $\alpha_c^{(1)}$ as a function of $1/N_b$. The NRG parameters are $\Lambda = 9.0$ and $M_s = 100$.

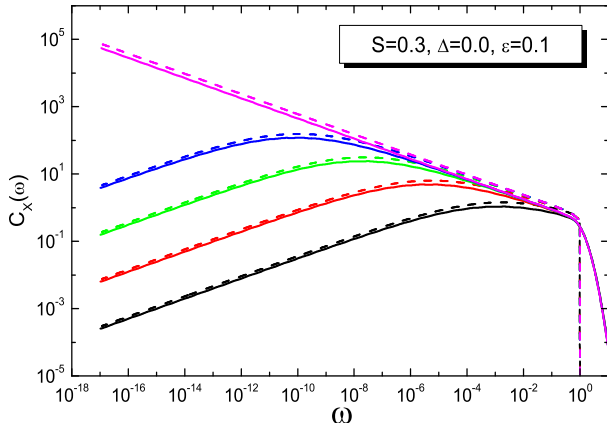


FIG. 14: $C_X(\omega)$ for $s = 0.3$, $\Delta = 0.0$ and $\epsilon = 0.1 > \epsilon_c$. The solid lines are NRG results and the dashed lines are exact ones. From bottom to top, $\alpha = \alpha_c - \delta\alpha$ with $\delta\alpha = 1.0 \times 10^{-2}$, 2.0×10^{-3} , 4.0×10^{-4} , 8.0×10^{-5} , and 0.0 . For NRG and the exact solution, we use respectively $\alpha_c^{NRG} = 0.085934484$ and $\alpha_c^{exc} = 0.075$. The NRG parameters are $\Lambda = 4.0$, $M_s = 100$, $N_b = 12$. The broadening parameter is $B = 1.0$.

expected. All the NRG results up to now point to the conclusion that $|\langle X \rangle| = \infty$ once the environment enters the unstable state, irrespective of the order of QPT's. This is consistent with the picture provided by the exact solution.

In Fig.14, we compare the NRG result for the dynam-

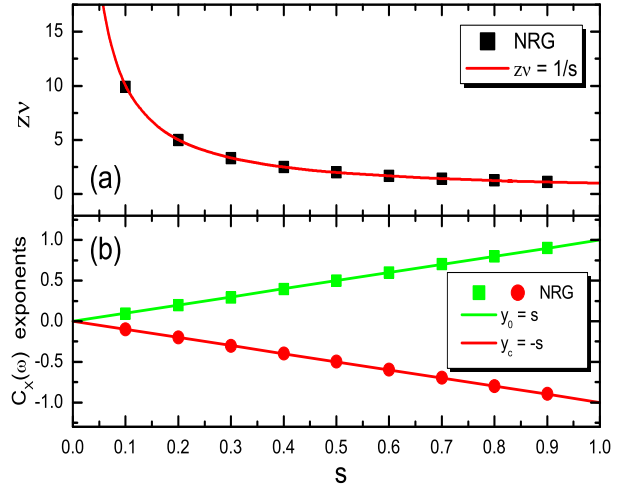


FIG. 15: Comparison of the universal exponents calculated from NRG and the exact ones. (a) The energy scale exponent $z\nu$. Symbols are NRG data and the solid line $z\nu = 1/s$ is from the exact solution; (b) exponents of $C_X(\omega)$: y_0 and y_c . Symbols are NRG data and the solid lines are exact results $y_0 = s$ and $y_c = -s$.

ical correlation function $C_X(\omega)$ with the exact one. Calculated at the same distance towards α_c^{NRG} and α_c^{exc} , respectively, the NRG results obtained using $\Lambda = 4.0$, $M_s = 100$, and $N_b = 12$ agree qualitatively with the exact solution Eq.(9), but smaller by 30% in magnitude. This error comes mainly from the discretization error and can be reduced by decreasing Λ to unity. In the low frequency limit, the power law behaviour ω^s for $\omega \ll \omega^*$ and ω^{-s} for $\omega \gg \omega^*$ are clearly seen, with a crossover scale ω^* moving towards zero as α approaches $\alpha_c^{(c)}$. The exact $C_X(\omega)$ curve has a sharp cut-off at $\omega = \omega_c$, inherited from the hard cut-off of $J(\omega)$ in Eq.(4). The long tail of the NRG curves in $\omega > 1.0$ is an artefact from the log-Gaussian broadening used in NRG.

In Fig.15, we compare the NRG exponents (solid symbols) with the analytical expressions (solid lines) in the range $0 < s < 1$. $z\nu$ shown in Fig.15(a) is the critical exponent of the crossover energy scale $T^* \propto |\alpha - \alpha_c^{(c)}|^{z\nu}$. The NRG data agree well with the exact exponent $z\nu = 1/s$. In Fig.15(b), the NRG result for the exponents y_0 and y_c are compared with the exact expressions $y_0 = s$ and $y_c = -s$. Here y_0 and y_c are the low frequency exponent of $C_X(\omega)$: $C_X(\omega) \propto \omega^{y_0}$ for $\alpha < \alpha_c^{(c)}$ and $C_X(\omega) \propto \omega^{y_c}$ at the critical point $\alpha = \alpha_c^{(c)}$.

In summary, in this Appendix we made detailed comparison between the NRG results and the exact solution for $\Delta = 0$ and quantitative agreement is achieved.

[1] A. O. Caldeira and A. J. Leggett, *Quantum Tunnelling in a Dissipative System*, Ann. Phys. **149**, 374 (1983).

[2] A. J. Leggett, S. Chakravarty, A. T. Dorsey *et al.*, *Dynamics of the Dissipative Two-State System*, Rev. Mod. Phys. **59**, 1 (1987).

[3] U. Weiss, *Quantum Dissipative Systems* (World Scientific, Singapore, 1999), 2nd edition.

[4] A. Garg, J. N. Onuchic, and V. Ambegaokar, *Effect of Friction on Electron Transfer in Biomolecules*, J. Chem. Phys. **83**, 4491 (1985).

[5] D. Xu and K. Schulten, *Multi-Mode Coupling of Protein Motion to Electron Transfer in the Photosynthetic Reaction Center: Spin-Boson Theory Based on a Classical Molecular Dynamics Simulation*, D. Xu and K. Schulten, in *The Photosynthetic Bacterial Reaction Center: II. Structure, Spectroscopy and Dynamics*, ed. J. Breton and A. Vermélio, (Plenum Press, New York, 1992).

[6] X. Song and A. A. Stuchebrukhov, *Outer-Sphere Electron Transfer in Polar Solvents: Quantum Scaling of Strongly Interacting Systems*, J. Chem. Phys. **99**, 969 (1993).

[7] L. Mühlbacher and R. Egger, *Electron Transfer Rates for Asymmetric Reactions*, Chem. Phys. **296**, 193 (2004).

[8] Y. Makhlin, G. Schön, and A. Shnirman, *Quantum-State Engineering with Josephson-Junction Devices*, Rev. Mod. Phys. **73**, 357 (2001).

[9] A. Shnirman, Y. Makhlin, and G. Schön, *Noise and Decoherence in Quantum Two-Level Systems*, Phys. Scr. T**102**, 147 (2002).

[10] M. H. Devoret, A. Wallraff, and J. M. Martinis, *Superconducting Qubits: A Short Review*, arXiv: cond-mat/0411174 (unpublished).

[11] J. Q. You and F. Nori, *Superconducting Circuits and Quantum Information*, Phys. Today **58**, 42 (2005).

[12] E. Novais and H. U. Baranger, *Decoherence by Correlated Noise and Quantum Error Correction*, Phys. Rev. Lett. **97**, 040501 (2006).

[13] R. Bulla, N. H. Tong, and M. Vojta, *Numerical Renormalization Group for Bosonic Systems and Application to the Sub-Ohmic Spin-Boson Model*, Phys. Rev. Lett. **91**, 170601 (2003).

[14] R. Bulla, H. J. Lee, N. H. Tong, and M. Vojta, *Numerical Renormalization Group for Quantum Impurities in a Bosonic Bath*, Phys. Rev. B **71**, 045122 (2005).

[15] S. Florens, D. Venturelli, and R. Narayanan, *Quantum Phase Transition in the Spin Boson Model*, Lect. Notes Phys. **802**, 145 (2010).

[16] N. Zhou *et al.*, *Ground-State Properties of Sub-Ohmic Spin-Boson Model with Simultaneous Diagonal and Off-diagonal Coupling*, Phys. Rev. B **90**, 155135 (2014).

[17] Y. Y. Zhang, Q. H. Chen, and K. L. Wang, *Quantum Phase Transition in the Sub-Ohmic Spin-Boson Model: an Extended Coherent-State Approach*, Phys. Rev. B **81**, 121105(R) (2010).

[18] C. Zhao, Z. Lü, and H. Zheng, *Entanglement Evolution and Quantum Phase Transition of Biased $s = 1/2$ Spin-Boson Model*, Phys. Rev. E **84**, 011114 (2011).

[19] M. F. Frenzel and M. B. Plenio, *Matrix Product State Representation without Explicit Local Hilbert Space Truncation with Applications to the Sub-Ohmic Spin-Boson Model*, New J. Phys. **15**, 073046 (2013).

[20] M. Vojta, *Impurity Quantum Phase Transitions*, Phil. Mag. **86**, 13 (2006).

[21] M. Vojta, N. H. Tong, and R. Bulla, *Quantum Phase Transitions in the Sub-Ohmic Spin-Boson Model: Failure of the Quantum-Classical Mapping*, Phys. Rev. Lett. **94**, 070604 (2005); *Erratum: Quantum Phase Transitions in the Sub-Ohmic Spin-Boson Model: Failure of the Quantum-Classical Mapping*, Phys. Rev. Lett. **102**, 249904(E) (2009).

[22] M. Vojta, R. Bulla, F. Gütte, and F. Anders, *Mass-Flow Error in the Numerical Renormalization-Group Method and the Critical Behavior of the Sub-Ohmic Spin-Boson Model*, Phys. Rev. B **81**, 075122 (2010).

[23] A. Winter, H. Rieger, M. Vojta, and R. Bulla, *Quantum Phase Transition in the Sub-Ohmic Spin-Boson Model: Quantum Monte Carlo Study with a Continuous Imaginary Time Cluster Algorithm*, Phys. Rev. Lett. **102**, 030601 (2009).

[24] A. Alvermann and H. Fehske, *Sparse Polynomial Space Approach to Dissipative Quantum Systems: Application to the Sub-Ohmic Spin-Boson Model*, Phys. Rev. Lett. **102**, 150601 (2009).

[25] C. Guo, A. Weichselbaum, J. von Delft, and M. Vojta, *Critical and Strong-Coupling Phases in One- and Two-Bath Spin-Boson Models*, Phys. Rev. Lett. **108**, 160401 (2012).

[26] N. H. Tong and M. Vojta, *Signatures of a Noise-Induced Quantum Phase Transition in a Mesoscopic Metal Ring*, Phys. Rev. Lett. **97**, 016802 (2006); L. B. Yu *et al.*, *Simulation of the Spin-Boson Model with Superconducting Phase Qubit Coupled to a Transmission Line*, Science-China **55**, 1557 (2012).

[27] A. Recati *et al.*, *Atomic Quantum Dots Coupled to a Reservoir of a Superfluid Bose-Einstein Condensate*, Phys. Rev. Lett. **94**, 040404 (2005).

[28] P. P. Orth, I. Stanic, and K. Le Hur, *Dissipative Quantum Ising Model in a Cold-Atom Spin-Boson Mixture*, Phys. Rev. A **77**, 051601(R) (2008).

[29] D. Porras, F. Marquardt, J. von Delft, and J. I. Cirac, *Mesoscopic Spin-Boson Models of Trapped Ions*, Phys. Rev. A **78**, 010101(R) (2008).

[30] D. Vion *et al.*, *Manipulating the Quantum State of an Electrical Circuit*, Science **296**, 886 (2002).

[31] P. Bertet, I. Chiorescu, G. Burkard G, *et al.*, *Dephasing of a Superconducting Qubit Induced by Photon Noise*, Phys. Rev. Lett. **95**, 257002 (2005).

[32] G. Ithier *et al.*, *Decoherence in a Superconducting Quantum Bit Circuit*, Phys. Rev. B **72**, 134519 (2005).

[33] F. Yoshihara *et al.*, *Decoherence of Flux Qubits due to $1/f$ Flux Noise*, Phys. Rev. Lett. **97**, 167001 (2006).

[34] K. Kakuyanagi *et al.*, *Dephasing of a Superconducting Flux Qubit*, Phys. Rev. Lett. **98**, 047004 (2007).

[35] K. D. Petersson, J. R. Petta, H. Lu, and A. C. Gossard, *Quantum Coherence in a One-Electron Semiconductor Charge Qubit*, Phys. Rev. Lett. **105**, 246804 (2010).

[36] G. Wolfowicz *et al.*, *Atomic Clock Transitions in Silicon-Based Spin Qubits*, Nat. Nanotechnol. **8**, 561 (2013).

[37] Y. Makhlin and A. Shnirman, *Dephasing of Solid-State Qubits at Optimal Points*, Phys. Rev. Lett. **92**, 178301 (2004).

[38] J. Bergli, Y. M. Galperin, and B. L. Altshuler, *Decoherence of a Qubit by non-Gaussian Noise at an Arbitrary*

Working Point, Phys. Rev. B **74**, 024509 (2006).

[39] L. Cywiński, *Dynamical-Decoupling Noise Spectroscopy at an Optimal Working Point of a Qubit*, Phys. Rev. A **90**, 042307 (2014).

[40] S. J. Balian, R. B. Liu, and T. S. Monteiro, *Keeping a Spin Qubit Alive in Natural Silicon: Comparing Optimal Working Points and Dynamical Decoupling*, Phys. Rev. B **91**, 245416 (2015).

[41] E. A. Muljarov and R. Zimmermann, *Dephasing in Quantum Dots: Quadratic Coupling to Acoustic Phonons*, Phys. Rev. Lett. **93**, 237401 (2004).

[42] Borri et al., *Ultralong Dephasing Time in InGaAs Quantum Dots*, Phys. Rev. Lett. **87**, 157401 (2001).

[43] M. F. Maghrebi, M. Krüger, and M. Kardar, *Flight of a Heavy Particle Nonlinearly Coupled to a Quantum Bath*, Phys. Rev. B **93**, 014309 (2016).

[44] K. G. Wilson, *The Renormalization Group: Critical Phenomena and Kondo Problem*, Rev. Mod. Phys. **47**, 773 (1975).

[45] R. Bulla, T. A. Costi, and Th. Pruschke, *Numerical Renormalization Group Method for Quantum Impurity Systems*, Rev. Mod. Phys. **80**, 395 (2008).

[46] A double-precision NRG calculation produces this splitting of degeneracy at the energy scale 10^{-15} . In Fig.3 and Fig.4, the flows are obtained from the quartic-precision calculation and the symmetry breaking is pushed to $N > 30$.

[47] Cowley, *Acoustic Phonon Instabilities and Structural Phase Transitions*, Phys. Rev. B **13**, 4877 (1976).

[48] V. Hizhnyakov, H. Kaasik, and I. Sildos, *Zero-Phonon Lines: The Effect of a Strong Softening of Elastic Springs in the Excited State*, Phys. Stat. Sol. (b) **234**, 644 (2002).

[49] D. C. Zheng and N. H. Tong, *Equilibrium Dynamics of the Sub-Ohmic Spin-Boson Model under External Bias*, unpublished.

[50] K. Le Hur, P. Doucet-Beaupré, and W. Hofstetter, *Entanglement and Criticality in Quantum Impurity Systems*, Phys. Rev. Lett. **99**, 126801 (2007).

[51] M. Haeberlein et al., *Spin-Boson Model with an Engineered Reservoir in Circuit Quantum Electrodynamics*, arXiv:1506.09114 (unpublished).

[52] T. Niemczyk et al., *Circuit Quantum Electrodynamics in the Ultrastrong-Coupling Regime*, Nature Physics **6**, 772 (2010).

[53] P. F. Diáz et al., *Observation of the Bloch-Siegert Shift in a Qubit-Oscillator System in the Ultrastrong Coupling Regime*, Phys. Rev. Lett. **105**, 237001 (2010).

[54] A. Baust et al., *Ultrastrong Coupling in Two-Resonator Circuit QED*, Phys. Rev. B **93**, 214501 (2016).

[55] B. Peropadre, P. F. Diáz, E. Solano, and J. J. García-Ripoll, *Switchable Ultrastrong Coupling in Circuit QED*, Phys. Rev. Lett. **105**, 023601 (2010).

[56] I. S. Gradshteyn and I. M. Ryzhik, *Table of Integrals, Series, and Products*, sixth edition, ed. A. Jeffrey and D. Zwillinger, (Academic Press, 2000). Entries 3.194-5, 9.100, 9.132-2, and 9.14.

[57] R. Bulla, Th. Pruschke, and A. C. Hewson, *Anderson Impurity in Pseudo-Gap Fermi Systems*, J. Phys.: Condens. Matter **9**, 10463 (1997).

[58] Yan-Hua Hou and Ning-Hua Tong, *Criticality of the Mean-Field Spin-Boson Model: Boson State Truncation and Its Scaling Analysis*, Euro. Phys. J. B **78**, 127 (2010).

[59] Ning-Hua Tong and Yan-Hua Hou, *Scaling Analysis in the Numerical Renormalization Group Study of the Sub-Ohmic Spin-Boson Model*, Phys. Rev. B **85**, 144425 (2012).